



**Multiscale Investigation of the Mechanism of Biomass
Deconstruction in the Dimethyl isosorbide/Water Co-
Solvent Pretreatment System**

Journal:	<i>Green Chemistry</i>
Manuscript ID	GC-ART-01-2024-000510
Article Type:	Paper
Date Submitted by the Author:	29-Jan-2024
Complete List of Authors:	Yang, shuang; Westlake University Mohan, Mood; Oak Ridge National Laboratory, Center for Molecular Biophysics; Joint BioEnergy Institute, Bioscience Gao, Xiangbo; Westlake University; Westlake Institute for Advanced Study; Zhejiang University Yang, Xianpeng; Westlake University Zhu, Jiawei; College of Chemistry and Materials Engineering Smith, Jeremy; Oak Ridge National Laboratory, UT/ORNL Center for Molecular Biophysics Wang, Lei; Westlake University; Westlake Institute for Advanced Study

Multiscale Investigation of the Mechanism of Biomass Deconstruction in the Dimethyl isosorbide/Water Co-Solvent Pretreatment System

Shuang Yang^{a,b,c,¥}, Mood Mohan^{d,¥}, Xiangbo Gao^{a,b,c}, Xianpeng Yang^{a,b}, Jiawei Zhu^e,

Jeremy C. Smith^f, Lei Wang^{a,b,*}

^a Key Laboratory of Coastal Environment and Resources of Zhejiang Province, School of Engineering, Westlake University, 18 Shilongshan Road, Hangzhou, 310024, Zhejiang Province, China

^b Institute of Advanced Technology, Westlake Institute for Advanced Study, 18 Shilongshan Road, Hangzhou, 310024, Zhejiang Province, China

^c College of Environmental and Resource Sciences, Zhejiang University, Hangzhou, 310058, Zhejiang Province, China

^d Biosciences Division and Center for Molecular Biophysics, Oak Ridge National Laboratory, Oak Ridge, Tennessee 37831, United States

^e College of Chemistry and Materials Engineering, Zhejiang A & F University, Hangzhou 311300, China

^f Department of Biochemistry and Cellular and Molecular Biology, University of Tennessee, Knoxville, Tennessee 37996, United States

¥ Equally contributed to the manuscript.

Corresponding author(s)

* E-mail: wang_lei@westlake.edu.cn (L. Wang)

Abstract

In the context of promoting a circular bioeconomy, the development of green and efficient lignocellulosic biomass pretreatment technologies so as to realize high value-added biomass utilization is of intense interest. We demonstrated the potential of the bio-based green solvent dimethyl isosorbide (DMI) for the fractionation of *Eucalyptus* biomass with excellent performance. Here, to investigate the mechanisms involved in biomass fractionation, microimaging and microspectroscopic techniques were employed together with molecular dynamics (MD) simulation and COSMO-RS quantum chemical calculations to derive multiscale information. Both the microstructure and regional chemistry of the cell wall vary significantly with the volume ratio of DMI/H₂O. The strongest effects were found at DMI/H₂O=9:1 and showed visible cell wall tearing cracks and cell wall deformation and collapse as well as the lowest values of cell wall thickness and circularity. From the MD simulations, lignin exhibits collapsed-like structure in pure H₂O with low solvent accessibility surface area (SASA) and radius of gyration (R_g). In contrast, lignin in DMI/H₂O shows extended structure with high SASA and solvent interactions dominated by van der Waals forces, with maximal contact in the 9:1 system. Further, the COSMO-RS calculated sigma (σ) potential suggests the intermolecular interactions in DMI and DMI/H₂O co-solvent are weak, leading to stronger interaction with lignin and correspondingly higher lignin dissolution. The radial distribution functions and σ -potential all show that again DMI/H₂O at 9:1 is an optimal volume ratio for high lignin dissolution. This study provides a solvent-ratio dependent mechanism for the action of polar aprotic solvents in the deconstruction of biomass.

Keywords

Lignocellulosic biomass, Organosolv pretreatment, Multiscale investigation, Deconstruction mechanism, Molecular simulation

1. Introduction

Lignocellulosic biomass pretreatment is one of the most crucial steps in a biomass refinery.^{1,2} In the last decades, several pretreatment methods have been developed.³ Of these, organosolv pretreatment is an emerging approach to obtain high-quality lignin and high-purity cellulose.^{4,5} In the context of promoting an eco-friendly and sustainable bioeconomy and to realize the clean separation and high value-added utilization of lignocellulosic biomass,⁶ as alternatives to conventional organic solvents, bio-based green solvents are being investigated, such as γ -valerolactone (GVL),⁷ dihydrolevoglucosenone (Cyrene)⁸ and dimethyl isosorbide (DMI).¹ Among these, DMI is an aprotic, water-miscible and non-toxic solvent which can be derived from D-glucose.⁹⁻¹² It is considered as one of the top 10 biobased platform chemicals.¹³ DMI was used in the field of lignocellulosic biomass pretreatment for the first time by our group.¹ In previous experimental and computational investigations,^{1,11} we demonstrated the potential of the DMI/H₂O co-solvent system for lignocellulosic biomass (*Eucalyptus*) fractionation. Under mild pretreatment conditions (120 °C, 60 min) and a volume ratio of DMI to H₂O of 9:1, the removal of lignin and hemicellulose reached more than 90% and 98%, respectively, and was better than those found for ratios of 10:0 (79.4%, 81.7%) and 8:2 (71.3%, 80.5%, see Table.S1 for evidence). Meanwhile, high-purity lignin was obtained, preserving a good fraction of β -O-4 linkages (~25%).

The mechanisms underlying the above results for DMI/H₂O pretreatment, including how DMI/H₂O co-solvent interacts with lignin and the role of H₂O in the co-solvent system, need to be elucidated. Current research on the deconstruction mechanisms of lignocellulosic biomass organosolv pretreatment has applied at least four main groups of approaches. The first is using microscopic imaging or microspectroscopic techniques to directly characterize changes in the composition and distribution of main components in cell walls.¹⁴ Xun Zhang¹⁵ used micro-Raman spectroscopy for quantitative visualization of the lignin from *Poplar* in various cell wall layers during delignification. A linear relationship between Raman intensity ratios and the lignin content (acquired by chemical compositions analysis) was established for the quantitative illustration of lignin removal in different cell wall layers. The second is using gas chromatography-mass spectrometry (GC-MS) to detect the structure and type of products, and

to infer possible degradation routes from the perspective of covalent bond breaking.¹⁶ For example, Jasiukaitytė et al.¹⁷ took benzyl phenyl ether (BPE) as a representative lignin model compound with the α -O-4 linkage, and investigated its reaction mechanism in sulfuric acid-acidified GVL and GVL/H₂O co-solvent via GC-MS. Results showed that the product distribution was strongly affected by H₂O, which was found to be of benefit in inhibiting the formation of larger lignin structures. The third is using the quantum-chemical computational COSMO-RS technique to study radial distribution functions (RDFs) reflecting microscopic interactions between lignin and the investigated solvent systems.¹⁸ For example, we computed the RDFs between lignin and a cyrene/H₂O co-solvent system at different molar ratios to understand the effects of various solvent/H₂O ratios on the solubility of the co-solvent system. Results showed that the higher contact probability of H₂O and lignin in cyrene/H₂O co-solvent at 4:1 molar ratio led to greater solvation of lignin molecules than at 1:1 and thus provides a preferred molar ratio for lignin dissolution.¹⁹ The fourth is using molecular dynamics (MD) simulation to study the behavior and conformation of lignin fragments in solution.^{20, 21} Vural et al.²² investigated the solvation of lignin polymers with different S/G/H compositions in co-solvents (H₂O, THF/H₂O and GVL/H₂O). Results showed that THF/H₂O and GVL/H₂O co-solvent were found to be “good” solvents for all types of lignin. In addition, the lignin solvent interactions, became slightly more favorable with increasing lignin methoxy substitution in GVL/H₂O co-solvent system, but did not vary in THF/H₂O co-solvent system. These indicate that the performance of lignin deconstruction and removal varies in different types of solvents. The above four groups of approaches focus on mechanisms at different scales and should be combined to optimally elucidate biomass deconstruction mechanisms in novel solvent-based systems.

The objectives of this work are to understand the deconstruction mechanism of the new DMI/H₂O co-solvent system for lignocellulosic biomass pretreatment at multiple scales, including macrostructural, cellular, subcellular and molecular scales. In addition, several unconventional characterization and analytical methods are used in this work. For example, we used an X-ray microscope to obtain both 3D and 2D structural changes of the biomass before and after pretreatment, as well as conductivity to reflect the free H⁺ concentration in the co-solvent system – an appropriate characterization method for solvent systems such as DMI for

which it is difficult to measure the pH. This study concentrates on a deep and systematic approach to analyze the deconstruction mechanism for biomass (Figure.1), and thus can provide a fundamental understanding for other bio-based polar non-protonic solvents like DMI used in the field of biomass pretreatment with a green and sustainable strategy.

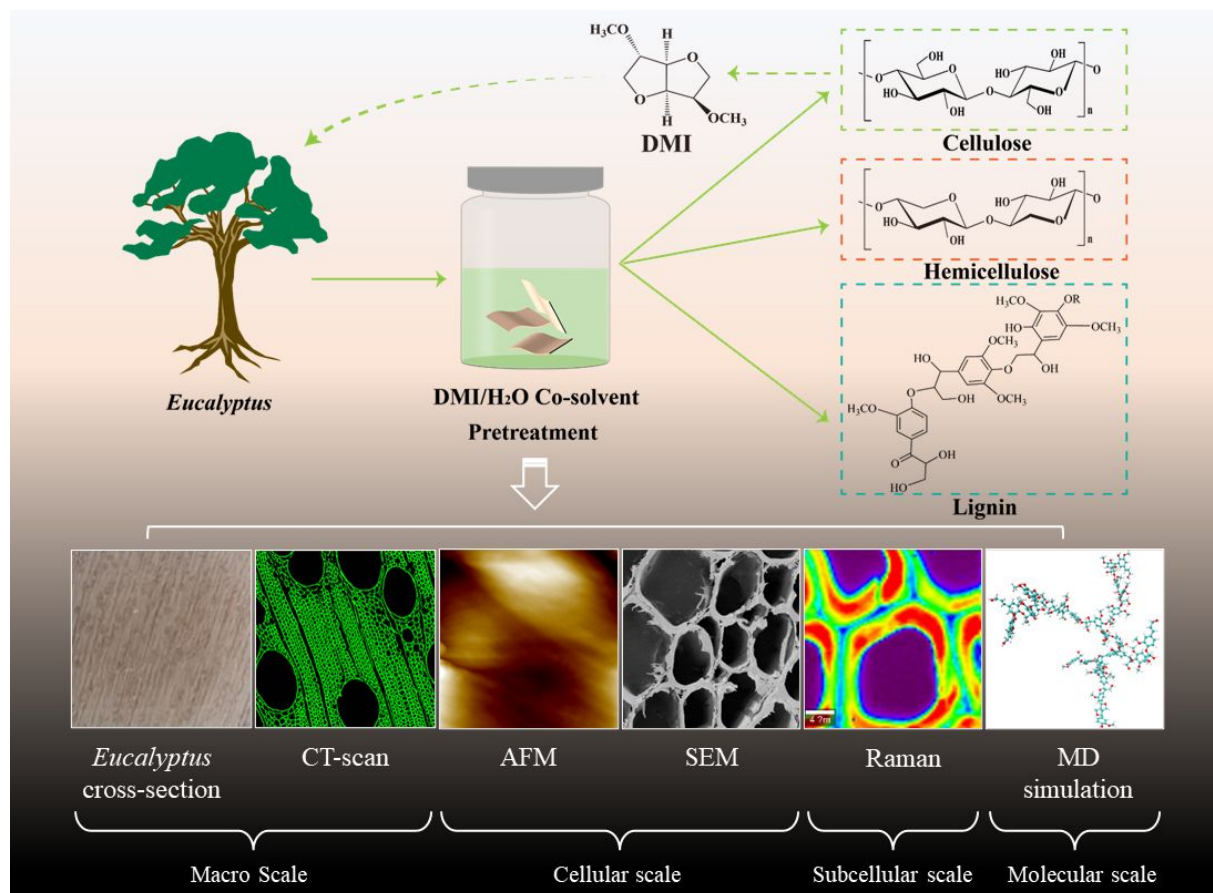


Figure.1 Multiscale investigation of the mechanism of biomass deconstruction in the DMI/H₂O co-solvent pretreatment.

2. Experimental and Computational Details

2.1 Materials and chemicals

Eucalyptus (*E. urophylla* × *E. grandis*) used in this study was obtained from Guangxi, China. Dimethyl sulfoxide (DMSO) was purchased from Sinopharm Holding Chemical Reagent Co., LTD. (Shanghai, China). Nail polish (H60100627) was provided by Nanjing Jiushan Chemical Co., LTD. (Nanjing, China). The specifications, models and procurement channels of other chemical drugs were the same as with our previous study.¹

2.2 *Eucalyptus* cross-section preparation and pretreatment

The secondary xylem of the *Eucalyptus* was cut into small pieces of 20 mm×10 mm×10 mm. After exhausting and softening treatment, the cross-sections with a thickness of 20 μm were prepared by using a microtome (LeicaSM2010R, Leica, Germany). The prepared *Eucalyptus* cross-sections were placed in a Synthware™ cylindrical pressure bottle with 15 mL of DMI-based co-solvent at different DMI to H₂O volume ratios (10:0, 9:1, 8:2) and 75 mM H₂SO₄. The samples were heated in Synthware™ aluminum blocks and reacted at 120 °C for keeping 60 min. After the reaction, the samples were cooled to room temperature (20 ± 5 °C), then soaked in the same proportion of co-solvent system for 12 h. After that, the cross-sections were soaked in dimethyl sulfoxide (DMSO) for 12 h, then soaked in Milli-Q for 12 h after washed repeatedly with Milli-Q for 3 times. The samples could be used for subsequent analysis and detection.

2.3 Characterization Methods

X-ray microscopy (XRM, Xradia 610 Versa, Zeiss, Germany) was used to characterize the two-dimensional (2D) and three-dimensional (3D) structural changes of the *Eucalyptus* cross-sections before and after DMI/H₂O co-solvent pretreatment. The freeze-dried samples were fixed on a plastic holder by double-sided adhesive tape. The current and voltage of the X-ray source were 71 μA and 70 kV, respectively. The detector 4X was chosen in the scan recipes, which means the optical magnification is 4. The pixel size was 0.78 μm and each CT image contained 1012*843 pixels. The phase segmentation and analysis of 2D cross-sections before and after pretreatment used the softwares ilastik²³ and Fiji/ImageJ.²⁴ The circularity was calculated using the following equation (1):²⁵

$$Circularity = \frac{4\pi A}{P^2} \quad (1)$$

where A and P are the area and perimeter of the cell lumens. Changes of surface morphology and roughness were detected using a field emission scanning electron microscopy (FE-SEM, Gemini 450, Zeiss, Germany) and atomic force microscope (AFM, Jupiter XR, Oxford, USA), respectively. The AFM testing was under the tap mode. The probe type was AC160TS-R3 with $f=300$ KHz, $C=26$ N/m, tip radius of 9 nm. *Eucalyptus* cross-sections were

fixed on a sample stage using double-sided adhesive tape before testing. The conductivity of different DMI/H₂O co-solvent systems was determined using a zeta potential analyzer (ZetaPALS, Brookhaven, USA) at 25 °C. The Raman spectra of *Eucalyptus* cross-sections were collected using a visible near infrared fast imaging Raman spectrometer (Alpha300R, WITec, Germany). The samples were fixed on slides, and then coverslips were placed on the samples and sealed with nail polish. Spectral calibration was performed with the Raman spectra of single crystal silicon before testing. The excitation wavelength, power and integral time were 532 nm, 20 w and 1.5 s, respectively. The surface fluorescence signals of samples were observed using a fluorescence microscope (Axio Zoom.V16, Zeiss, Germany). The samples were prepared in the same way with the Raman spectroscopy analysis. Dual-channel observation (Green Fluorescent Plot and DsRed Fluorescent Plot) was chosen, with excitation wavelengths of 488 nm and 545 nm and emission wavelengths of 509 nm and 572 nm, and the exposure time was 1.5 s. The milled wood lignin was prepared by ball milling and dioxane extraction,²⁶ as well as the lignin solubility at 30 °C was measured according to a previously reported method.²⁷

2.4 Molecular Dynamics Simulations

The lignin model polymer for MD simulations was taken from our previous studies,^{11, 28, 29} where the lignin molecule was generated using the Lignin Builder^{28, 30} with a molecular weight of ~5 kDa (and the degree of polymerization is 26). For all the investigated molecules, CHARMM force field parameters were used, and the force field parameters for lignin, water, and DMI were taken from our earlier work.^{11, 29} In our recent studies, we validated the DMI force field parameters against experimental densities and experimental Hansen solubility parameters.¹¹ Therefore, further validation of force field parameters has not been performed in the present study.

To study the microscopic interactions and structural changes of lignin in different DMI/H₂O co-solvent system, MD simulations were carried out using the NAMD package.³¹ The initial configuration for all the investigated systems was prepared according to the molar ratio of DMI and H₂O (DMI/H₂O molar ratios = 1:0, 1.1:1, 1:2, and 1:8 corresponding to volume ratios = 10:0, 9:1, 8:2, and 1:1) using PACKMOL.³² The simulation details, such as

the number of solvent molecules, lignin molecules, and final box size are summarized in Table.S2. The potential energy of the system was first minimized for 200 000 steps using a steepest-descent algorithm. The system was then heated and equilibrated for 15 ns under the NPT ensemble using the Langevin thermostat and Nose-Hoover Langevin barostat.^{33, 34} With a tolerance of 10^{-5} , the SHAKE algorithm was implemented to constrain all the hydrogen involved bonds.³⁵ The Particle Mesh Ewald (PME) method was implemented to treat long-range electrostatic interactions at a cut-off distance of 12 Å with an accuracy of 10^{-6} (PME tolerance).³⁶ Three separate production runs with a time length of 500 ns were performed on each simulated system, starting with a different initial velocity distribution. At every 5 ps, the production coordinates were saved for structural and dynamics analysis. A 2 femtoseconds (fs) time step was used to integrate the equations of motion. All MD simulation trajectories were visualized and analyzed using TCL scripts, and Visual Molecular Dynamics (VMD) tool.^{37, 38} The non-bonded interaction energies between lignin and DMI/H₂O co-solvent were calculated per mole of lignin. The calculation formulas of non-bonded interaction energies between lignin and DMI/H₂O co-solvent in the support information.

2.5 COSMO-RS Calculations

The chemical structures of DMI and H₂O were drawn using Avogadro.³⁹ In our earlier studies, the COSMO files of DMI and H₂O were generated using the BVP86/TZVP/DGA1 level of quantum chemical theory and basis set, and the same COSMO files were used in the present study.^{11, 40-42} The generated COSMO files were utilized in the COSMOtherm package (version 21)^{43, 44} to calculate the sigma (σ -) potentials of the isolated and DMI/H₂O mixtures, and partition coefficient of DMI in octanol/water with BP_TZVP_21 parametrization. The σ -profiles of mixtures of DMI/H₂O at different molar ratios were calculated as the mole-fraction-weighted sum of the σ -profiles of their individual components.^{45, 46} Further, using the σ -profiles of solvent mixtures, the σ -potentials of mixture can be calculated. Calculation of partition coefficients using the COSMO-RS model was discussed in detail elsewhere.^{47, 48}

3. Results and discussion

3.1 Changes in 3D cellular morphology of *Eucalyptus* cross-sections

Our previous results showed that DMI/H₂O co-solvent pretreatment significantly altered

the composition of lignin, hemicellulose and cellulose in the samples, removing over 90% of the lignin and almost all of the hemicellulose.¹ Changes in the content of these components are likely to correspond to changes in the macrostructure and microstructure of the samples. X-ray microscope has high resolution and non-destructive stereo reconstruction micro-imaging capability, as well as can characterize both 3D and 2D structures of the samples. The internal 3D microstructure of the samples can be constructed with sub-micron precision.

The 3D macrostructures of the *Eucalyptus* cross-sections before and after DMI/H₂O pretreatment obtained by X-ray microscopy are in Figure.S1. The segmented 3D structures (Figures 2a-2d) and raw images (Figures 2e-2h) show the effect of pretreatment. Foreign matter was found (blue arrow in Figure.2b) generated on the surface of *Eucalyptus* cross-section pretreated with the condition of pure DMI (10:0), which may be due to lignin microspheres formed during the pretreatment process being deposited on the surface of the samples. The sample pretreated at DMI/H₂O=9:1 showed visible cell wall tearing cracks (yellow arrow in Figure.2c) and cell wall deformation and collapse (red arrow in Figure.2c), which was beneficial for raw materials fractured into much smaller fibrillar particle during the pretreatment process.¹ In contrast, the *Eucalyptus* cross-section pretreated under the condition of DMI/H₂O=8:2 (Figure.2d) did not differ significantly from that of the raw material (Figure.2a).

In order to understand the changes in cell wall morphology more accurately, changes in the cell wall thickness and roundness before and after pretreatment were analyzed (200 cells in the white rectangles area in Figure.2 (e, f, g, h)) using the software ImageJ (Figure.2i and Figure.2j). Circularity reflects the degree of cell wall deformation: the smaller the circularity the greater the deformation.²⁵ From Figure.2i and Figure.2j, it can be seen that after pretreatment, the cell wall thickness and circularity values were reduced, and trends of changes in two indicators were consistent. The more obvious change was the samples under the condition of DMI/H₂O=9:1 with the lowest values of cell wall thickness and circularity, meaning that the samples under this condition had the highest lignin and hemicellulose removal efficiencies, consistent with our previous experimental findings.¹ In addition, the cell wall thickness and circularity of the samples pretreated under the 10:0 condition were slightly higher than those under the 8:2 condition, but these differences were not significant.

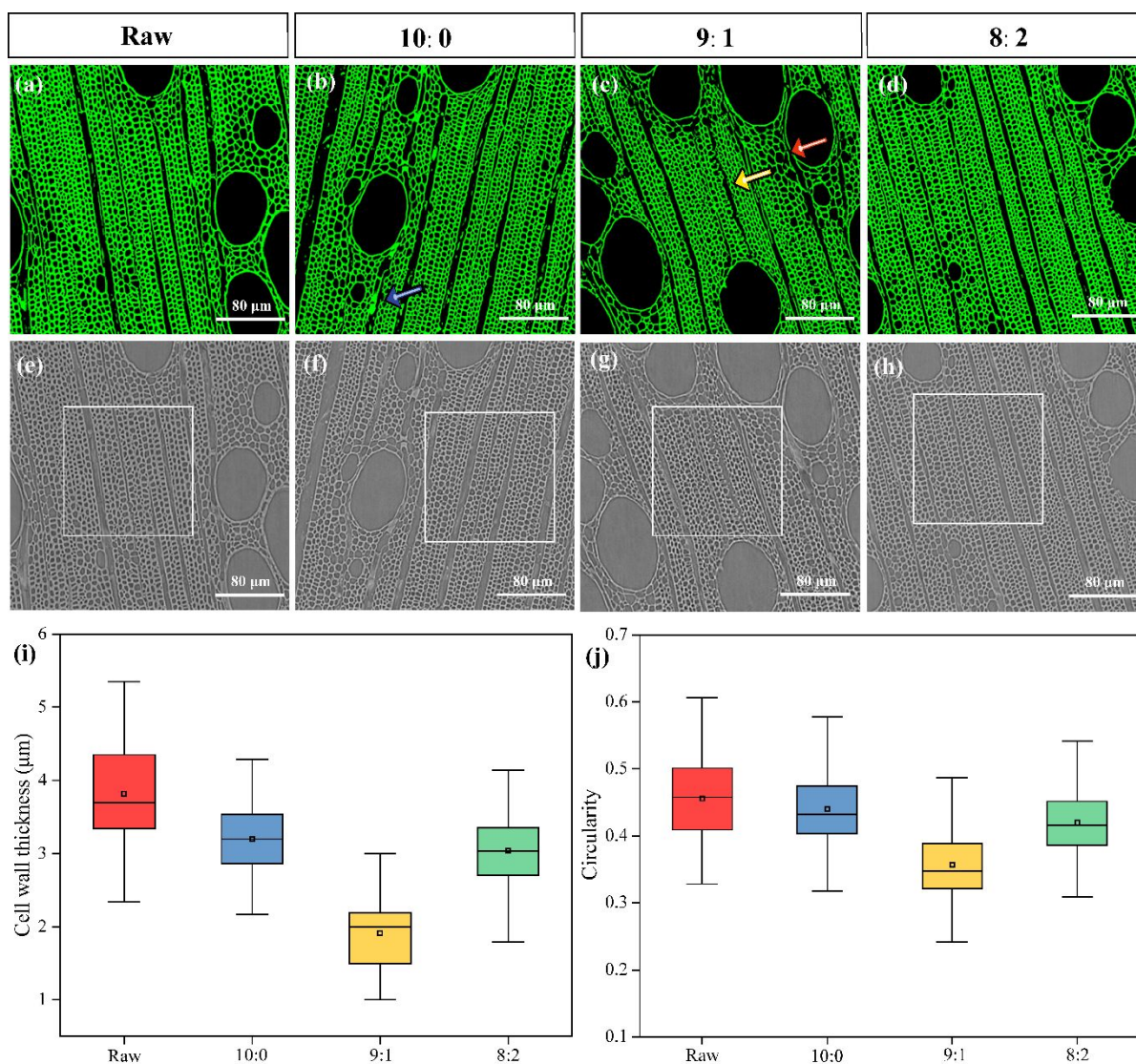


Figure.2 X-ray microscopy images of the *Eucalyptus* cross-sections before and after DMI/H₂O co-solvent pretreatment. (a,b,c,d) Binarized images (obtained with the help of ilastik and Fiji/ImageJ software). (e,f,g,h) 2D original images. Changes of cell wall thickness (i) and circularity (j).

3.2 Changes in morphology of *Eucalyptus* cross-sections

In general, wood cross-sections were found to undergo a variety of changes in their apparent morphology after the DMI/H₂O pretreatment, including cell collapse, wood fibers breaking and surface roughness and color changes.⁴⁹⁻⁵¹ Figure.3 shows apparent morphologies of raw and pretreated *Eucalyptus* cross-sections (10:0, 9:1, 8:2) in circle images (Figure.3 (a, b, c, d)). One visible change was that the surface color of *Eucalyptus* slices changed from milky white to yellowish brown after pretreatment with DMI/H₂O (10:0), mainly due to structural changes of lignin during *Eucalyptus* pretreatment.⁵² Previous studies have shown that the β-

O-4 bond in the lignin structure was broken into ketones by acidification during the pretreatment process,^{53, 54} which accelerated the degradation and condensation of lignin, forming color-emitting groups such as Hibbert ketones, quinones and quinone methyl groups.⁵² The second change was that the surface of *Eucalyptus* slices became rougher after pretreatment, mainly due to the removal of lignin and hemicellulose during the solvent pretreatment. The components on the surface of the wood slices were more likely to be preferentially removed, which led to the roughness of the wood slice surfaces. In order to quantify the roughness of the samples before and after sample pretreatment, *Eucalyptus* slices before and after pretreatment were analyzed using AFM. Figure.3 (a, b, c, d), (e, f, g, h) & (i, j, k, l) are images after magnification of 2, 4 and 50 times, respectively. From the 2x and 4x images it can be found that the deformation of the cell wall was most obvious after the pretreatment under the 9:1 condition with the roughness as 74.743 nm, consistent with the degree of delignification results.¹

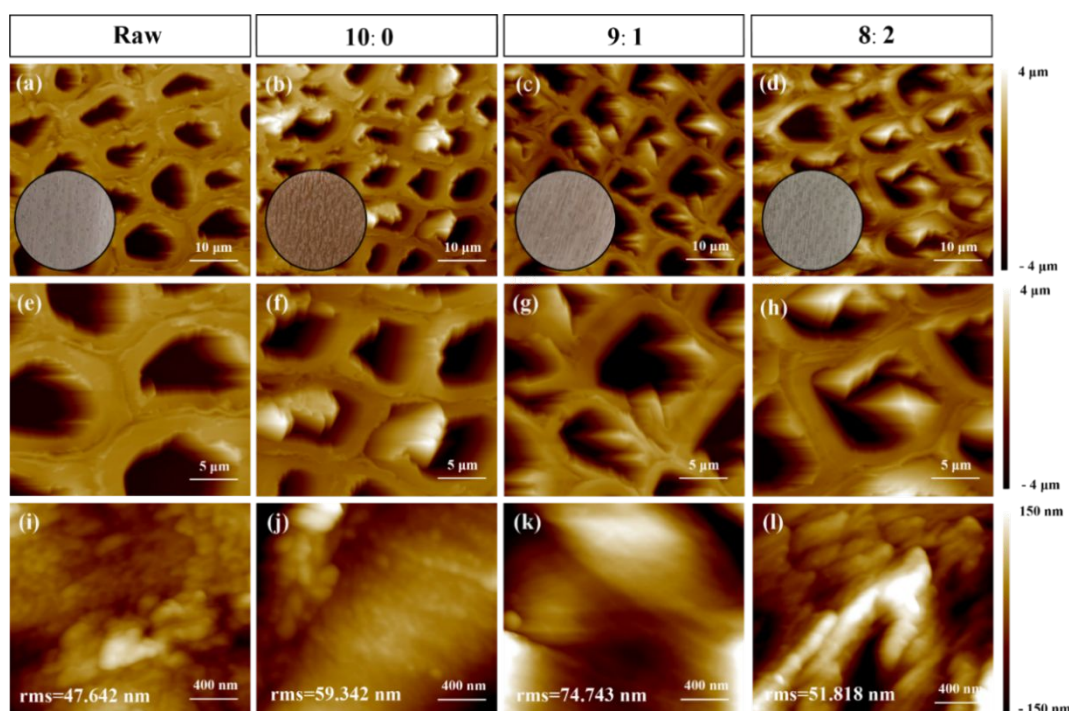


Figure.3 Images of raw and pretreated *Eucalyptus* cross-sections and changes of cell wall roughness of *Eucalyptus* cross-sections before and after pretreatment.

3.3 Changes in the microstructure of *Eucalyptus* cell wall

Figure.3 shows the changes in the apparent color and surface roughness of the samples

but does not yield information about the cell-wall microstructure. Therefore, FE-SEM was applied (Figure.4). The untreated *Eucalyptus* had a dense structure, and the regions between the cell corner middle lamella (CCML) and the compound middle lamella (CML) were completely filled. On further magnification to 4000x (Figure.4b), it was observed that the untreated *Eucalyptus* cell wall was intact, with a smooth and dense surface on the cross-section and a flat inner cell wall. After pretreatment with different DMI/H₂O co-solvent systems for 60 min, the cell wall structure of *Eucalyptus* changed to different degrees. The most severe deformation of the cell wall occurred under the condition of DMI/H₂O=9:1, and the highest lignin removal efficiency (91.2%)¹ was observed under this condition, only leaving a thin cellulose skeleton (Figure.4c and Figure.4g). In addition, the deposition of lignin microspheres on the surface of the sample treated with pure DMI (Figure. 4f) was observed, confirming the presence of foreign substances on the surface of the sample captured by X-ray microscopy (Figure.2b). Theoretically, if the DMI/H₂O co-solvent systems with different ratios had the same deconstruction mechanism, the changes in cell wall thickness should be proportional to the total removal efficiency of lignin and hemicellulose. However, this was not the case, the levels of lignin and hemicellulose removal efficiency (Table.S1) being 9:1 (91.2%, 98.6%) > 10:0 (79.4%, 81.7%) > 8:2 (71.3%, 80.5%),¹ whilst that of cell wall thickness was 10:0 (Figure.4f) > 8:2 (Figure.4h) > 9:1 (Figure.4g). These results imply that the lignin at the cell corner (CC) was preferentially removed in the pure DMI (10:0) system. Only in this way may the thickness of the cell wall under the condition of 10:0 still be higher than 8:2, even if the lignin removal efficiency under the condition of 10:0 is higher than 8:2.

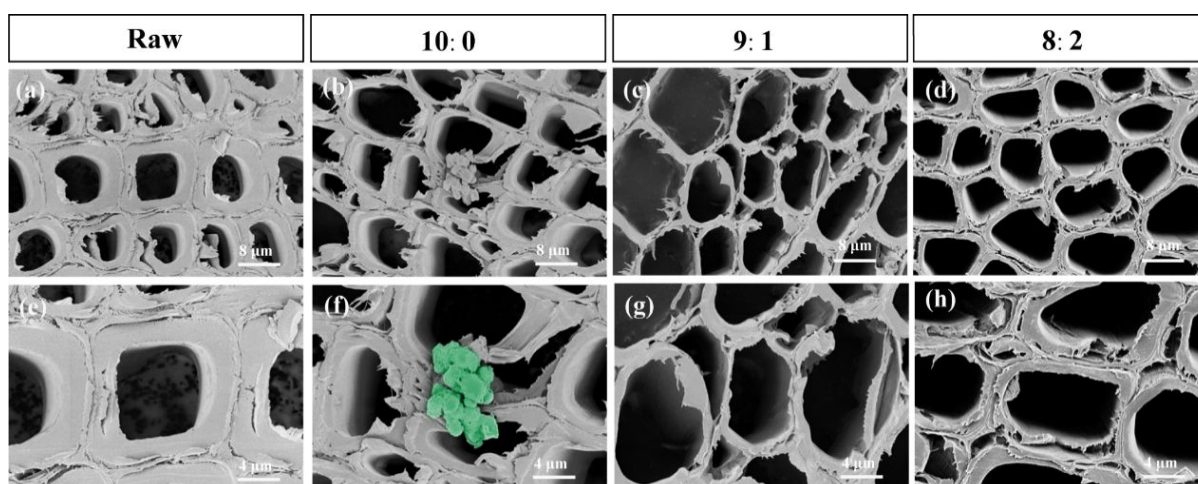


Figure.4 Microstructure of *Eucalyptus* cell wall before and after DMI/H₂O co-solvent pretreatment by FE-SEM (Figure. 4f was colorized to indicate the deposited lignin particles).

3.4 Changes in the cell wall region chemistry of *Eucalyptus* cross-sections

Confocal Raman microscopy was utilized to investigate the distribution of the main chemical components of the cell wall during the pretreatment, with a view to analyzing the above phenomena from the changes of subcellular scale. The assignments of the characteristic peaks of the main components in the cell wall are summarized in Table.S3. The Raman shifts of cellulose mainly occurred at 2897 cm⁻¹, and the characteristic peaks of lignin mainly occurred at 1605 cm⁻¹ and 1660 cm⁻¹. Therefore, the spectral integration of 2840-2920 cm⁻¹ can be used to obtain Raman imaging of cellulose distribution in the cell wall of *Eucalyptus*, and the spectral integration for 1600-1680 cm⁻¹ can be used to obtain the lignin distribution. The results are shown in Figure.5. The distribution of cellulose in untreated *Eucalyptus* (Figure.5a) was heterogeneous in different regions, the highest concentration of cellulose being in the region of the secondary wall, followed by the region of the CML, and the region of the CCML. As lignin was removed from the samples after pretreatment, the strength of cellulose gradually increased, with the highest concentration of cellulose in the secondary wall of *Eucalyptus* under the 9:1 condition (Figure.5b), and it also can be seen that the cell wall occurred a severe deformation and the wood fibers were fractured in this condition.

For the distribution of lignin in the cell wall of untreated *Eucalyptus* (Figure.5d), the region with the highest concentration was the CCML region, followed by the CML region and the lowest concentration was found in the secondary wall region. After DMI/H₂O co-solvent pretreatment, the lignin distribution trends were very different and the signal intensity was reduced to different degrees. There was still a strong lignin signal present at the CCML under the condition of 8:2. Thus, the decrease of lignin concentration under this condition mainly originated from the lignin removal in the region of secondary wall, which indicates that the dissolution of lignin located in the secondary wall region was more pronounced than in the CCML region under this condition. One possible explanation for this phenomenon is the solvent permeation mechanism, which allowed the solvent to permeate from the lumen to the CCML and then to the cell wall, and thus preferential delignification might occur in the

secondary wall region.⁵⁵ This explanation is supported by the laxity of the cell walls, which peeling away from each other in Figure.4d and Figure.4h. The cell wall was also found to be more lax in the secondary wall region than in the CCML region.⁵⁵ When the volume ratio of DMI to H₂O in the co-solvent system was 9:1, the lignin signal almost disappeared (Figure.5e), indicating that most of lignin was removed under this condition. In addition, we also found that the resolution of the component distribution images was decreased after co-solvent pretreatment, mainly due to the erosion of the sample surface during the solvent pretreatment, which resulted in a rougher surface compared to the original (Figure.3). We were unable to obtain Raman spectra of the samples in pure DMI (10:0) because the strong fluorescence signal (wavelength around at 600 nm) under this condition had obscured the Raman signal on the sample surface. Lignin itself was auto-fluorescent.^{56, 57} Normally, the auto-fluorescence intensity is positively proportional to the concentration of lignin, so the lignin concentration can be indirectly estimated by the change of fluorescence intensity under the same exposure time. Therefore, a change of fluorescence intensity on the surface of *Eucalyptus* cross-section before and after DMI/H₂O co-solvent pretreatment was observed, as shown in Figure.S2. The changes of green fluorescence were consistent with the trend of the removal efficiency of the lignin under different conditions. However, the trend of the red fluorescence intensity on the surface of pretreated *Eucalyptus* cross-section was different from that of the green fluorescence intensity, mainly because the fluorescence intensity of the sample treated with the 10:0 condition was uniform and stronger than that of the raw sample, which is the direct reason why no Raman signal was observed on the sample surface under this condition. Lähdetie et al.⁵⁸ also investigated the reason why samples containing lignin produce laser-induced fluorescence (LIF) that overlaps with the Raman band. By analyzing the Raman spectra of lignin dimer model compounds, results showed that the molecular structure and conformation were key factors influencing the fluorescence intensity. The same reason can also explain the phenomenon in this experiment, as it was found that the lignin in the cellulose-rich pulp under 10:0 condition occurred severe condensation in our previous work.¹

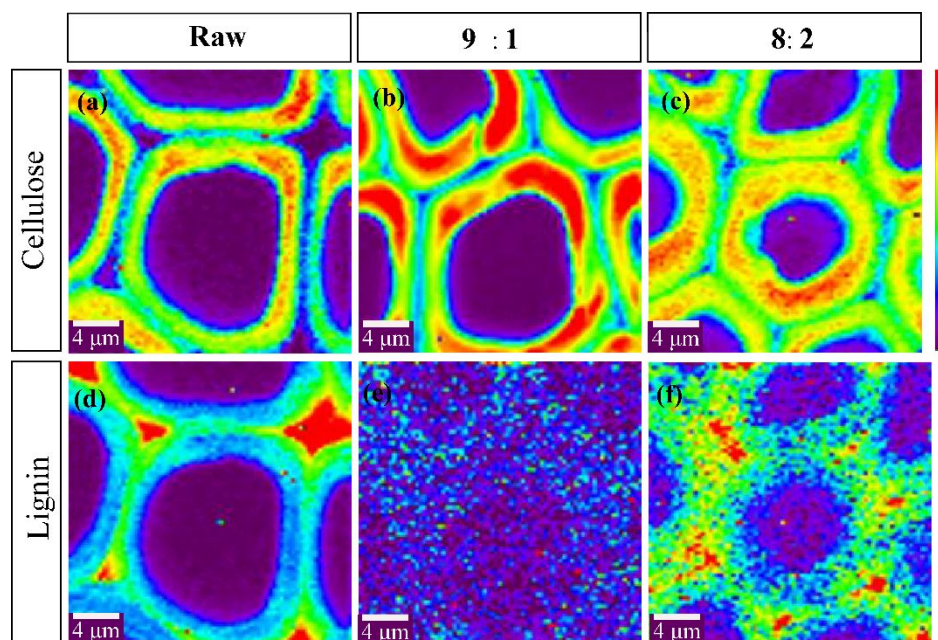


Figure.5 Raman imaging of lignin and cellulose distribution in *Eucalyptus* cell walls before and after DMI/H₂O co-solvent pretreatment. (a) Raw_cellulose. (b) 9:1_cellulose. (c) 8:2_cellulose. (d) Raw_lignin. (e) 9:1_lignin. (f) 8:2_lignin.

From the above experimental phenomena, both the microstructure and regional chemistry of the cell wall were very different under the different pretreatment conditions, reflecting that the DMI/H₂O co-solvents correspond to different delignification mechanisms at different volume ratios of DMI to H₂O. It can be inferred that the efficient removal of lignin from *Eucalyptus* slices under pure DMI (10:0) conditions mainly depends on the solubilization of DMI, but only dissolving the CCML region and some regions that were easily penetrated by DMI. In contrast, under 8:2 conditions (more H⁺ free in the co-solvent system), dominated by the breaking of covalent bonds (benzyl ether bonds, phenyl glycosidic bonds and γ ester bonds, etc.) within the LCC molecule, the addition of H₂O leads to a poor lignin solubility in the DMI/H₂O co-solvent system. Thus, based on the experimental results a hypothesis can be proposed that the efficient removal of lignin should be a balanced process between the breaking of LCC bonds, the solubilization of lignin degradation fragments and their stability in the co-solvent system.

3.5 Conductivity of different DMI/H₂O co-solvent systems

During the acid catalyzed solvent pretreatment, the LCC bond breaking in biomass was mainly related to the free H⁺ concentration in the co-solvent system.⁵⁹ Therefore, it was

necessary to quantify the free H^+ concentration in the co-solvent system. DMI is a polar non-protonic solvent and hard to ionize, and thus it is difficult to measure the pH of the co-solvent. However, it is possible to reflect the relative free H^+ concentration by measuring the conductivity of different co-solvent systems, and the result of this is shown in Table.1. The conductivities of both pure H_2O and DMI are all nearly $0 \mu S/cm$. When $75 \text{ mM } H_2SO_4$ was added to the pure DMI (0:10) system, the conductivity of the solvent is only $0.6 \mu S/cm$, close to zero. However, when $75 \text{ mM } H_2SO_4$ was added to the pure H_2O (0:10) system, the conductivity of the system reached more than $40,000 \mu S/cm$. This result illustrates that the removal of lignin in the pure DMI mainly relies on DMI to dissolve the lignin out of the cell wall, because there was no free H^+ present in the solvent system. Furthermore, the conductivity of the co-solvent system was found to increase gradually with the increase of the H_2O content in the co-solvent system, from $0.6 \mu S/cm$ in 10:0, $225.6 \mu S/cm$ in 9:1 to $1591.7 \mu S/cm$ in 8:2. It can be seen that the different contents of H_2O in the co-solvent system lead to different concentrations of free H^+ , which also implies that the ability of different co-solvent systems to break LCC bonds in the biomass is different.

Table.1 Conductivity of DMI, H_2O , and different DMI/ H_2O co-solvents volume ratios.

DMI/ H_2O ratio	Conductivity ($\mu S/cm$)
10:0	0.6
9:1	225.6
8:2	1591.7
0:10	42287.2

3.6 Dissolution mechanism of lignin in the DMI/ H_2O co-solvent system from MD simulations

To understand the dissolution mechanism of lignin, the solubility of milled wood lignin was tested (Figure.S3). The results show that the solubilities of 10:0 and 9:1 are similar, both slightly higher than that of 8:2. In addition, MD simulations were performed with DMI/ H_2O at

different DMI/H₂O volume ratios at 10:0 (neat DMI), 9:1, 8:2, 1:1 and 0:10 (neat water). The MD simulation data for pure DMI (10:0) and H₂O (0:10) were taken from our previous work.¹¹

To assess the compactness of the lignin structures, the radius of gyration (R_g) of lignin in different DMI/H₂O co-solvent systems environments was calculated for the last 150 ns of the production runs. Figure.6a shows the probability distribution of the R_g of lignin in DMI, H₂O, and DMI/H₂O co-solvent systems. The average R_g values were 9.75 Å, 16.45 Å, and ~15.83 Å for the H₂O, DMI, and DMI/H₂O co-solvent systems, respectively. The lower and narrowly distributed R_g values in H₂O indicates a collapsed structure. In contrast, the R_g values of lignin in the DMI and DMI/H₂O co-solvent systems are considerably higher, indicating that lignin adopts a more extended structure. These observations are corroborated by visual inspection of representative snapshots from the simulations (Figure.S4). In addition to R_g , the solvent-accessible surface area (SASA) is a useful property for measuring the interface between a solute and its solvent *i.e.*, the surface area of solute that in contact with the solvent. The probability distributions of the lignin SASA are shown in Figure.6b. The SASA is higher in the DMI and DMI/H₂O co-solvent systems than in H₂O, implying that lignin is more accessible to DMI and DMI/H₂O. The characteristics of the SASA probability distributions resemble those observed for R_g .

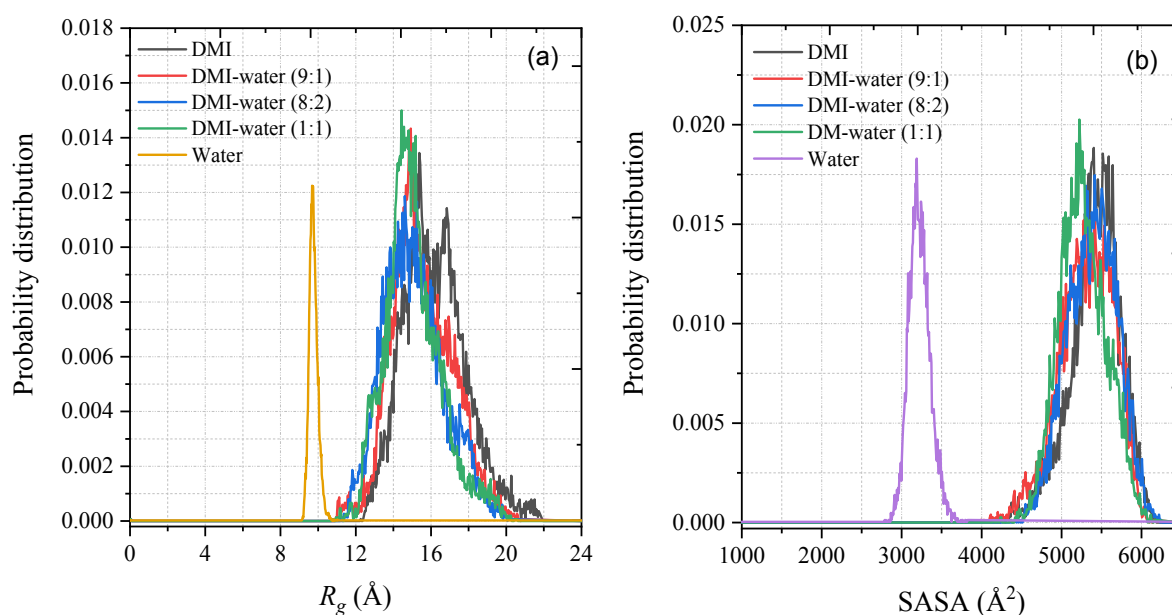


Figure.6 Probability distributions of the (a) radius of gyration (R_g) and (b) SASA for the lignin polymer in different DMI/H₂O co-solvent systems environments.

As the concentration of H₂O increases, DMI and H₂O were found to phase separate at 8:2 and 1:1 volume ratio of DMI to H₂O (Figure.S5). Although the delignification of biomass in 8:2 and 1:1 volume ratios of DMI to H₂O is lower than in pure DMI (10:0)¹ and DMI/H₂O water 9:1, the R_g and SASA of lignin are similar. This is mainly due to the lignin being fully solvated by DMI in all three systems. To further examine the phase separation of DMI and H₂O, COSMO-RS calculations were performed to calculate the octanol/water partition coefficient. The resulting value of 1.25 confirms the hydrophobic nature of DMI. Since lignin has aromatic rings and does not tend to interact with H₂O, DMI better solvates the polymer and results in increased SASA and configurational extension (Figure.S6). Thus, the R_g and SASA of lignin are higher in DMI/H₂O at 8:2 and 1:1 than in pure water.

To gain further insights into the energetics of the lignin-solvent interactions the non-bonded interaction energy between the lignin and solvent molecules was calculated. The total non-bonded interaction energy is a sum of electrostatic and van der Waals (vdW) terms. The results are given in Figure.7. Due to the significant presence of both hydrophilic and hydrophobic sites on lignin, both electrostatic and van der Waals interactions play an important role in its interaction with DMI/H₂O.^{11, 60, 61} In contrast, in the cases of cellulose and hemicellulose, electrostatic interactions govern the dissolution process.^{62, 63}

Figure.7 shows that the total interaction energy is roughly constant with DMI concentration. However, the highest interaction energy for lignin was obtained in DMI/H₂O at 9:1 volume ratio (*i.e.*, -668.72 kcal/mol), consistent with the highest delignification of the biomass. Strikingly, in the DMI systems vdW interactions dominate the interaction energies. In contrast, for lignin-H₂O the interaction energy is dominated by electrostatics and the contribution of vdW interaction is much smaller. The strong vdW interaction energy between lignin and DMI is surface-area dependent and leads to extended polymer structures.^{11, 28} A representation of an MD snapshot for lignin-DMI/H₂O is shown in Figure.S6. DMI tends to make stronger interactions with lignin aromatic rings, while water interacts with lignin through hydrogen bonds.

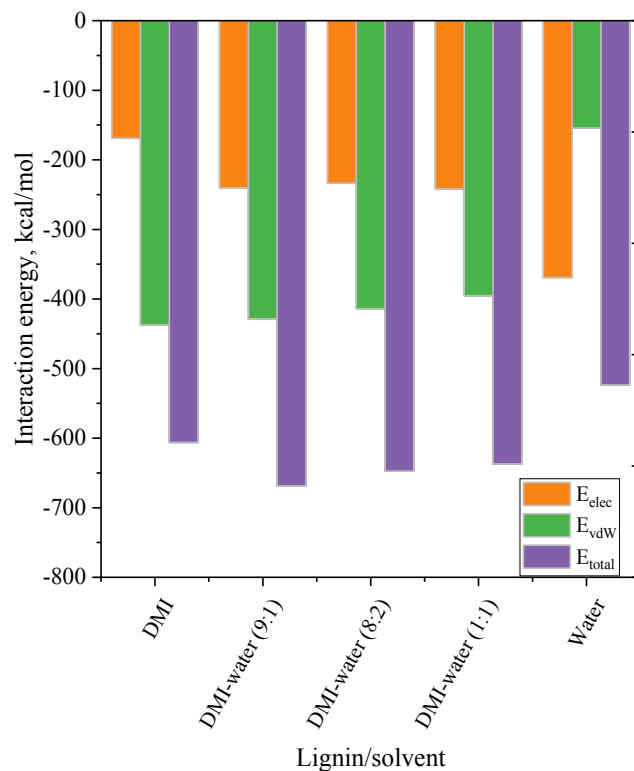


Figure.7 Nonbonded interaction energies between the lignin polymer and solvent species computed by MD simulations.

Next, to derive local structural features, radial distribution functions (RDF; $g(r)$) were computed between lignin and the DMI/H₂O co-solvent systems. The RDFs between the lignin oxygen (O) and the O (acceptor) atoms of DMI or H₂O are depicted in Figure.8. Figure.8a shows the RDF at different volume ratios. The first and highest solvation peak between lignin and DMI is at 3.45 Å, indicating that DMI forms well-defined coordination around lignin. The height of RDF peak $g(r)$ for lignin/DMI (10:0) is ~1.2, implying that the contact-pair formation between lignin and DMI molecules is stronger in the first solvation shell (3.45 Å) than at 9:1 and 8:2 volume ratios. The RDF for the second and third solvation shells (5.5 Å and 6.5 Å) and beyond for lignin/DMI are dominated by DMI/H₂O at 9:1. In the case of lignin/H₂O (0:10), the H₂O molecule approaches lignin moiety most frequently at a distance of 2.85 Å in all systems (Figure.8b), and the H₂O molecules are again well ordered around the lignin. In pure H₂O (0:10) system and in DMI/H₂O at 1:1 volume ratio, the lignin/H₂O RDF peak height is ~0.6-1, while the $g(r)$ height in DMI/H₂O at 9:1 is ~2.8, indicating that the contact-pair number between lignin and H₂O in DMI/H₂O at 9:1 is much higher (2-5 times greater) than in pure H₂O or a 1:1 volume ratio of DMI to H₂O, and also 2 times greater than DMI/H₂O at 8:2. The

higher contact-pair in the 9:1 volume ratio leads to higher polarity of DMI/H₂O at 9:1, thereby increasing the dissolution of lignin. This was further correlated with the COSMO-RS calculated sigma (σ)-potentials and experimentally measured Kamlet-Taft parameters.^{27,28} From Figure.8, it is interesting to observe that the first solvation shell peak between lignin-DMI is at 2.70 Å, while for lignin and water this is at 2.85 Å, indicating that lignin is more closely approached by DMI (see Figure.S4 for evidence).

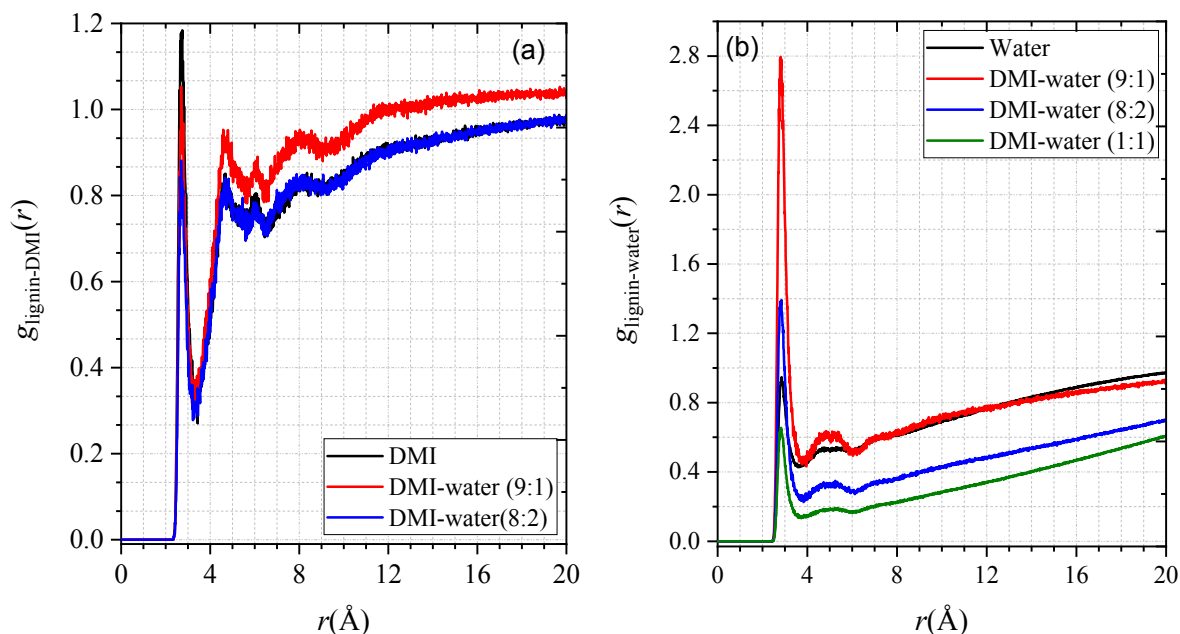


Figure.8 Radial distribution function (RDF) plot between the O atom of lignin and (a) the O1 atom of DMI, (b) the O atom of H₂O in pure and DMI/H₂O co-solvent systems.

In the COSMO-RS analysis, the σ -potential measures the affinity of a molecule to a surface of polarity σ , which provides insights into a solvent's interactions with itself and in a mixture.⁴⁵ As shown in Figure.9, we categorize the σ -potential into three regions: affinity to interact with HB acceptor ($\sigma > +0.01$ e/Å²), affinity to interact with HB donor ($\sigma < -0.01$ e/Å²), and non-polar (-0.01 e/Å² $< \sigma < +0.01$ e/Å²) regions.⁶⁴ In the σ -potential plot, the negative value of chemical potential ($\mu(\sigma)$) indicates a molecule rich with acceptor or donor sites, while positive $\mu(\sigma)$ signifies a lack of acceptor or donor surfaces.^{19, 45} For H₂O, COSMO-RS calculations yield a symmetric σ -potential with negative $\mu(\sigma)$, meaning intermolecular interactions between the H₂O molecules are strong (HB acceptor regions interact with HB donor region). In contrast, the σ -potentials of DMI and the DMI/H₂O co-solvent are asymmetric, and the values of $\mu(\sigma)$ are more negative in the negative charge density region

($\sigma > -0.01 \text{ e}/\text{\AA}^2$), which implies that DMI and DMI/H₂O co-solvent have a higher affinity to interact with H-bond donor surfaces than water. The σ -potentials of DMI and DMI/H₂O are positive or less negative in the large positive region of screening charge densities ($\sigma > +0.01 \text{ e}/\text{\AA}^2$), which corresponds to the DMI and DMI/H₂O co-solvent systems lacking H-bonding donor sites. Thus, the intermolecular interaction in DMI and DMI/H₂O co-solvent is very weak, leading to stronger interaction with lignin and correspondingly higher lignin dissolution.

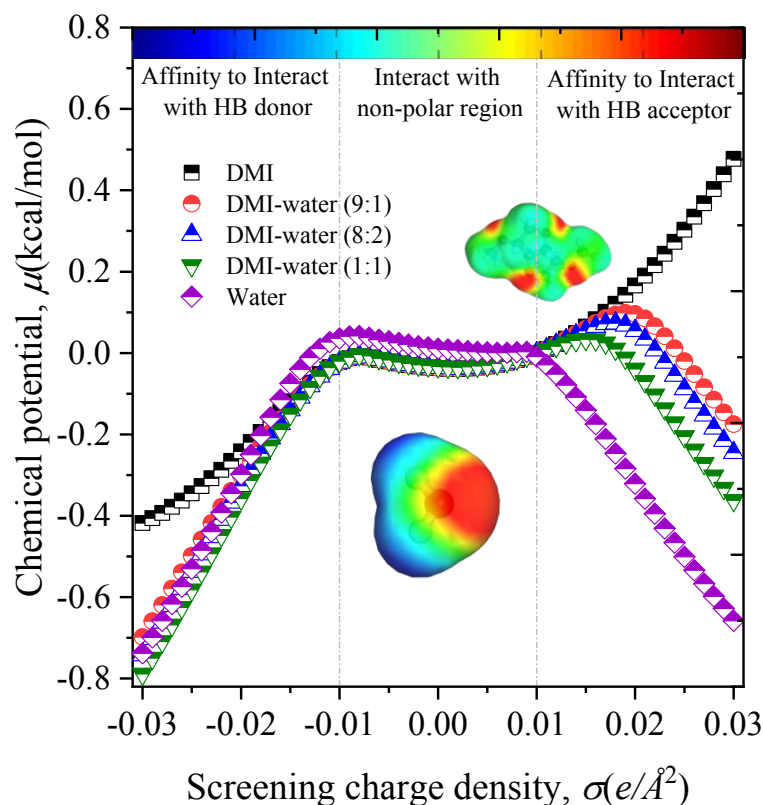


Figure.9 COSMO-RS-calculated sigma (σ)-potentials of H₂O, DMI, and DMI/H₂O co-solvent systems.

A closer look at Figure.9 shows that the σ -potential of DMI/H₂O co-solvent in the H-bond acceptor region ($\sigma > -0.01 \text{ e}/\text{\AA}^2$) is more negative than for DMI, implying that the DMI/H₂O co-solvent exhibits higher hydrogen bonding acceptor capability than does pure DMI. Yu *et al.* (2023)²⁷ reported the Kamlet-Taft parameters of DMI/H₂O co-solvent systems at different volume ratios, and found the hydrogen basicity (β) of DMI/H₂O at 9:1 volume ratio to be higher ($\beta=1.04$) than for pure DMI and DMI/H₂O co-solvent at 8:2, indicating that DMI/H₂O at 9:1 has a high interaction affinity with lignin. The σ -potentials and Kamlet-Taft parameters of DMI/H₂O at 9:1 volume ratio are consistent with each other and with the MD calculated RDF

and interaction energies. Therefore, of those tested both experimentally and theoretically, DMI/H₂O at 9:1 volume ratio has the greatest capacity to dissolve lignin.

4. Conclusions

In this work, biomass cross-sections before and after pretreatment with the DMI/H₂O co-solvent system were characterized and analyzed at multiple length scales using a variety of microimaging and microspectroscopic technologies and with computational chemistry. The experimental results indicate that both the microstructure and regional chemistry of the cell wall are very different under the different pretreatment conditions, reflecting different delignification mechanisms at various volume ratios of DMI to H₂O.

The addition of H₂O changes the free H⁺ concentration as demonstrated by the conductivity measurements and the lignin solubility as revealed by solubility test as well as computational simulations. In pure DMI, lignin dissolution removal is sufficient in the CCML region, where lignin is more accessible than in other regions, due to the excellent lignin solubility of DMI, although its free H⁺ concentration is low. Under 8:2 conditions, where higher free H⁺ concentration favors covalent bond cleavage, lignin removal is limited by its poor ability to dissolve lignin. The role of water in affecting lignin solubility was further demonstrated by MD simulations and COSMO-RS calculations. The MD results showed that as the H₂O concentration increases, a phase separation occurs under the 8:2 condition, which limits the accessibility of solvent to cell wall components and thus results in a poor lignin removal efficiency. In contrast, 9:1 provides the optimum conditions for biomass delignification, combining effective bond breaking and superior lignin dissolution due to stronger interaction energies and higher contact pair formation (RDF analysis) between lignin and DMI/H₂O with higher hydrogen bond acceptor capacity (COSMO-RS analysis).

In conclusion, microscopic visualization of cell walls from the micrometer to the nanometer scale provides information on the spatial, morphological and chemical changes of cell walls before and after DMI/H₂O co-solvent pretreatment. Combining these observations, conductivity measurements, solubility tests and MD simulations, we have shown that the efficient removal of lignin is a balanced process between the breaking of LCC bonds, the solubilization of lignin degradation fragments and their stability in the co-solvent system. As a

part of future work, we are exploring the different solvent recovery routes and evaluating the environmental and economic performances of DMI/H₂O co-solvent based biorefinery designs. This study thus provides a fundamental understanding of the multiscale results on the biomass deconstruction mechanism by solvent DMI. These knowledge and approaches take will contribute to the research field with regards to discover and understand the green, efficient and sustainable lignocellulosic biomass pretreatment technologies and the promotion of their large-scale realization.

Acknowledgement

This project was supported by the foundation of the Natural Science Foundation of China (No. 22378333), Zhejiang Provincial Department of Science and Technology (2023SDXHDX0006), Westlake Education Foundation and the Research Center for Industries of the Future (RCIF) at Westlake University. This work was also supported by the U. S. Department of Energy (DOE), Office of Science, through the Genomic Science Program, Office of Biological and Environmental Research (contract no. FWP ERKP752). The authors would like to acknowledge the Instrumentation and Service Center for Molecular Sciences and the Instrumentation and Service Center for Physical Sciences at Westlake University for most of the characterizations conducted in this study, as well as would like to acknowledge Prof. Guangcai Chen and Dr. Shihao Su for improving the manuscript.

Conflicts of interest

There are no conflicts to declare.

Reference

1. S. Yang, X. Yang, X. Meng and L. Wang, *Green Chemistry*, 2022, **24**, 4082-4094.
2. H. Q. Lê, A. Zaitseva, J.-P. Pokki, M. Ståhl, V. Alopaeus and H. Sixta, *ChemSusChem*, 2016, **9**, 2939-2947.
3. A. Sidana and S. K. Yadav, *Journal of Cleaner Production*, 2022, **335**, 130286.
4. S. C. Rabelo, P. Y. S. Nakasu, E. Scopel, M. F. Araújo, L. H. Cardoso and A. C. d. Costa, *Bioresource Technology*, 2023, **369**, 128331.
5. N. Aggarwal, P. Pal, N. Sharma and S. Saravanamurugan, *ACS Omega*, 2021, **6**, 27247-27258.
6. Y. Jiang, X. Wang, Z. Meng, M. Zhang, S. Wang and X. Liu, *Green Chemistry*, 2024, DOI: 10.1039/D3GC04029A.
7. D. M. Alonso, S. H. Hakim, S. Zhou, W. Won, O. Hosseinaei, J. Tao, V. Garcia-Negron, A. H. Motagamwala, M. A. Mellmer, K. Huang, C. J. Houtman, N. Labbé, D. P. Harper, C. T. Maravelias, T. Runge and J. A. Dumesic, *Science Advances*, 2017, **3**, e1603301.
8. X. Meng, Y. Pu, M. Li and A. J. Ragauskas, *Green Chemistry*, 2020, **22**, 2862-2872.
9. F. Russo, F. Galiano, F. Pedace, F. Aricò and A. Figoli, *ACS Sustain. Chem. Eng.*, 2019, **8**, 659-668.
10. M. Annatelli, D. Dalla Torre, M. Musolino and F. Aricò, *Catalysis Science & Technology*, 2021, **11**, 3411-3421.
11. M. Mohan, K. L. Sale, R. S. Kalb, B. A. Simmons, J. M. Gladden and S. Singh, *ACS Sustain. Chem. Eng.*, 2022, **10**, 11016-11029.
12. S. Yang, Y. Wang, X. Kang, X. Yang, C. Zhang, L. Deng, X. Meng, X. Song and L. Wang, *Industrial Crops and Products*, 2023, **203**, 117169.
13. J. J. Bozell and G. R. Petersen, *Green chemistry*, 2010, **12**, 539-554.
14. X. Zhang, L. Li and F. Xu, *Forests*, 2022, **13**, 439.
15. X. Zhang, *RSC Advances*, 2021, **11**, 13124-13129.
16. S. Li, C. Zhao, F. Yue and F. Lu, *Polymers*, 2020, **12**, 116.
17. E. Jasiukaitytė-Grojzdek, M. Huš, M. Grilc and B. Likozar, *ACS Sustainable Chemistry & Engineering*, 2020, **8**, 17475-17486.
18. M. Mohan, H. Choudhary, A. George, B. A. Simmons, K. Sale and J. M. Gladden, *Green Chemistry*, 2021, **23**, 6020-6035.
19. M. Mohan, K. L. Sale, R. S. Kalb, B. A. Simmons, J. M. Gladden and S. Singh, *ACS Sustainable Chemistry & Engineering*, 2022, **10**, 11016-11029.
20. S. V. Pingali, M. D. Smith, S.-H. Liu, T. B. Rawal, Y. Pu, R. Shah, B. R. Evans, V. S. Urban, B. H. Davison, C. M. Cai, A. J. Ragauskas, H. M. O'Neill, J. C. Smith and L. Petridis, *Proceedings of the National Academy of Sciences*, 2020, **117**, 16776-16781.
21. L. Petridis and J. C. Smith, *Nature Reviews Chemistry*, 2018, **2**, 382-389.
22. D. Vural, J. C. Smith and L. Petridis, *Green Chemistry*, 2020, **22**, 4331-4340.
23. S. Berg, D. Kutra, T. Kroeger, C. N. Straehle, B. X. Kausler, C. Haubold, M. Schiegg, J. Ales, T. Beier, M. Rudy, K. Eren, J. I. Cervantes, B. Xu, F. Beuttenmueller, A. Wolny, C. Zhang, U. Koethe, F. A. Hamprecht and A. Kreshuk, *Nature Methods*, 2019, **16**, 1226-1232.
24. J. Schindelin, I. Arganda-Carreras, E. Frise, V. Kaynig, M. Longair, T. Pietzsch, S. Preibisch, C. Rueden, S. Saalfeld, B. Schmid, J.-Y. Tinevez, D. J. White, V. Hartenstein, K. Eliceiri, P. Tomancak and A. Cardona, *Nature Methods*, 2012, **9**, 676-682.
25. J. P. Lancha, P. Perré, J. Colin, P. Lv, N. Ruscassier and G. Almeida, *Scientific Reports*, 2021, **11**, 8444.

26. D. S. Zijlstra, C. W. Lahive, C. A. Analbers, M. B. Figueirêdo, Z. Wang, C. S. Lancefield and P. J. Deuss, *ACS Sustainable Chemistry & Engineering*, 2020, **8**, 5119-5131.
27. H. Yu, Z. Xue, Y. Wang, C. Yan, L. Chen and T. Mu, *Separation and Purification Technology*, 2023, **306**, 122688.
28. M. Mohan, B. A. Simmons, K. L. Sale and S. Singh, *Sci. Rep.*, 2023, **13**, 271.
29. M. Mohan, K. X. Huang, V. R. Pidatala, B. A. Simmons, S. Singh, K. L. Sale and J. M. Gladden, *Green Chem.*, 2022, **24**, 1165-1176.
30. J. V. Vermaas, L. D. Dellon, L. J. Broadbelt, G. T. Beckham and M. F. Crowley, *ACS Sustainable Chemistry & Engineering*, 2019, **7**, 3443-3453.
31. J. C. Phillips, R. Braun, W. Wang, J. Gumbart, E. Tajkhorshid, E. Villa, C. Chipot, R. D. Skeel, L. Kale and K. Schulten, *Journal of computational chemistry*, 2005, **26**, 1781-1802.
32. L. Martínez, R. Andrade, E. G. Birgin and J. M. Martínez, *Journal of computational chemistry*, 2009, **30**, 2157-2164.
33. S. E. Feller, Y. Zhang, R. W. Pastor and B. R. Brooks, *J. Chem. Phys.*, 1995, **103**, 4613-4621.
34. G. J. Martyna, D. J. Tobias and M. L. Klein, *J. Chem. Phys.*, 1994, **101**, 4177-4189.
35. M. P. Allen and D. J. Tildesley, *Computer simulation of liquids*, Oxford University Press, New York, 1987.
36. S. W. Deleeuw, J. W. Perram and E. R. Smith, *Proc. R. Soc. London, Ser. A*, 1983, **388**, 177-193.
37. W. Humphrey, A. Dalke and K. Schulten, *J. Mol. Graph.*, 1996, **14**, 33-38.
38. M. Brehm and B. Kirchner, *J. Chem. Inf. Model.*, 2011, **51**, 2007-2023.
39. M. D. Hanwell, D. E. Curtis, D. C. Lonie, T. Vandermeersch, E. Zurek and G. R. Hutchison, *J. Cheminformatics*, 2012, **4**, 17.
40. M. Mohan, T. Banerjee and V. V. Goud, *Journal of Chemical and Engineering Data*, 2016, **61**, 2923-2932.
41. Y.-R. Liu, K. Thomsen, Y. Nie, S.-J. Zhang and A. S. Meyer, *Green Chemistry*, 2016, **18**, 6246-6254.
42. M. Gonzalez-Miquel, M. Massel, A. DeSilva, J. Palomar, F. Rodriguez and J. F. Brennecke, *J. Phy. Chem. B*, 2014, **118**, 11512-11522.
43. Y. Y. Li and Y. Y. Jin, *Renew Energ*, 2015, **77**, 550-557.
44. F. Eckert and A. Klamt, *AIChE J.*, 2002, **48**, 369-385.
45. A. Klamt and F. Eckert, *Fluid Phase Equilibria*, 2000, **172**, 43-72.
46. J. Palomar, J. S. Torrecilla, J. Lemus, V. R. Ferro and F. Rodríguez, *Physical Chemistry Chemical Physics*, 2008, **10**, 5967-5975.
47. M. Zawadzki, K. Padaszynski, M. Krolikowska and E. Grzechnik, *J. Mol. Liq.*, 2020, **307**, 112914.
48. L. Christoph and K. Andreas, 2014.
49. B. Sundqvist and T. Morén, *Holz als Roh- und Werkstoff*, 2002, **60**, 375-376.
50. I. Kaur and G. Sahni, *Green and Sustainable Chemistry*, 2018, **08**, 92-114.
51. J. Jiang, J. Wang, X. Zhang and M. Wolcott, *Industrial Crops and Products*, 2017, **97**, 498-508.
52. X. Wang, Q. Hou, X. Zhang, Y. Zhang, W. Liu, C. Xu and F. Zhang, *International Journal of Biological Macromolecules*, 2020, **157**, 673-679.
53. S.-N. Sun, H.-Y. Li, X.-F. Cao, F. Xu and R.-C. Sun, *Bioresource Technology*, 2015, **176**, 296-299.
54. J. Li, G. Henriksson and G. Gellerstedt, *Bioresource Technology*, 2007, **98**, 3061-3068.
55. Z. Ji, J. Ma and F. Xu, *Microsc Microanal*, 2014, **20**, 566-576.
56. T. Auxenfans, C. Terryn and G. Paës, *Scientific Reports*, 2017, **7**, 8838.
57. J. Ralph, *Phytochemistry Reviews*, 2010, **9**, 65-83.

58. A. Lähdetie, P. Nousiainen, J. Sipilä, T. Tamminen and A.-S. Jääskeläinen, *Holzforschung*, 2013, **67**, 531-538.
59. S. An, W. Li, Q. Liu, M. Li, Q. Ma, L. Ma and H.-m. Chang, *RSC Advances*, 2017, **7**, 32452-32460.
60. M. Mohan, H. Choudhary, A. George, B. A. Simmons, K. Sale and J. M. Gladden, *Green Chem.*, 2021, **23**, 6020-6035
61. M. K. Konduri, F. Kong and P. Fatehi, *Eur. Polym. J.*, 2015, **70**, 371-383.
62. M. Mohan, T. Banerjee and V. V. Goud, *ChemistrySelect*, 2016, **1**, 4823-4832.
63. M. Mohan, P. Viswanath, T. Banerjee and V. V. Goud, *Mol. Phys.*, 2018, **116**, 2108-2128.
64. E. C. Achinivu, M. Mohan, H. Choudhary, L. Das, K. Huang, H. D. Magurudeniya, V. R. Pidatala, A. George, B. A. Simmons and J. M. Gladden, *Green Chemistry*, 2021, **23**, 7269-7289.